Seismic Imaging Of an Intracrustal Deformation In the Northwestern Margin Of the South China Sea: the Role Of a Ductile Layer In the Crust

Haibo Huang[1,3], Frauke Klingelhoefer[2], Xuelin Qiu[1,3,4], Yuhan Li[1,4], Ping Wang[1,3]

[1]Key Laboratory of Ocean and Marginal Sea Geology, South China Sea Institute of Oceanology, CAS, Guangzhou, P.R. China.

[2]Department of Marine Geosciences, IFREMER, Plouzané, France.

[3]Innovation Academy of South China Sea Ecology and Environmental Engineering, Chinese Academy of Sciences, Guangzhou 510301, China

[4]College of Earth and Planetary Sciences, UCAS, Beijing, P.R. China

Corresponding author: Xuelin Qiu (xlqiu@scsio.ac.cn)

Key Points:

- Intracrustal deformation that includes detached upper crust and ductile lower crust was imaged across the Zhongsha Trough, a rift valley.
- Prominent magmatism in the OCT lead to a rapid onset of the embryonic oceanic crust mixed with the highly fractured continental crust.
- Partially serpentinized upper mantle beneath the OCT indicates short-term fault activity before the oceanic spreading.

Abstract

The continental margins of the South China Sea (SCS) have undergone episodic rifting since the Cenozoic, and there are great divergences in processes of the crustal deformation and seafloor opening. In this work, we present a P-wave velocity model starting from north of Xisha Trough to Zhongshanan Basin in the northwestern SCS margin by modeling the ocean bottom seismometers data of a wide-angle seismic profile OBS2013-1. The results show that the crust thins symmetrically across the western Xisha Trough, from more than ~20 km at the flanks to ~10 km in the central valley where the sedimentary layers thicken to over 6 km. In the Zhongsha Trough closer to the deep basin, the upper crust is detached in a ~20 km wide region and the lower crust is intruded by volcanism and has seismic velocities increased by more than ~0.3 km/s. The volcanic intrusion was blocked by a shearing boundary between the brittle and ductile crust. A ~50 km wide ocean-continent transition region beneath the Zhongshanan Basin is underlain by ~6 km thick continental crust and shows high magnetic anomalies related to early stage magmatism and magnetized upper mantle. These observations, together with plate reconstructions based on gravity and magnetic analysis, suggest that the continental margin was deformed by crustal detachment and prominent magmatism that was followed by a rapid accretion of the oceanic crust.

1 Introduction

The South China Sea (SCS) has been widely recognized as a Cenozoic marginal basin developed from atypical magma-poor passive rifting (Taylor and Hayes, 1983). Depending on lithologic composition, rheology and thermal structure of the continental lithosphere, passive margins can undergo progressive extension in variable styles of crustal deformation (Huismans and Beaumont, 2014). Over the years, geophysical surveys have revealed an asymmetrical

conjugate pattern and the depth-related lithospheric extension of the margins in the SCS (Franke et al., 2014; Huismans and Beaumont, 2014; Huang et al., 2019). However, the rupture mode of the continental crust and the growing processes of the oceanic crust are still highly controversial. In 2017, the 367/368 IODP drillings have been conducted in deep water (> 3000 m; Fig. 1) at the edge of the northern margin of the SCS to reveal the nature of the transitional structures from continent to ocean (Jian et al. 2018; Sun et al. 2018). The coring data suggest that the SCS has experienced fast lithospheric extension without mantle exhumation (Larsen et al., 2018), very different from the well-established findings along the Atlantic Ocean margins (Dean et al., 2000). In addition, early-stage magmatism prior to steady-state seafloor accretion was detected overlying hyper-thinned continental crust (~8 km thick) and showing an east to west propagation based on interpretation of reflection seismic profiles (Larsen et al., 2018). Accordingly, interlayer decoupling in the lithosphere could have been facilitated when the pre-rupture magmatism heating up and reducing the crustal viscosity (Franke et al., 2014).

The lithology measurements of the sampled rocks should be implemented combining closely with deep structure detection such as the geophysical exploration. The obtained seismic structures will provide an explanation for the rheological behavior of the continental crust (e.g., the weak zones and interlayer decoupling) that finally determines the transition pattern from rifting to rupturing (Huismans and Beaumont, 2014). Moreover, original architecture and thermal structure of the crust usually evolved during poly-phased extension (Brune et al., 2014), and it requires a comparison of the deforming expressions in time and space. In this work, we present a P-wave velocity model from a wide-angle seismic survey starting from the slope area in the northwestern margin of the SCS to the south of the Zhongsha Bank (Macclesfield Bank; Fig. 1b). Seismic travel times were modeled to image the rift-related structures e.g. brittle/ductile behavior

of the continental crust, and thus to provide further insights into the crustal deformation during rifting. The crusts show a regional deformation pattern in the failed rifts, and hyper-thinned continental crust in the ocean-continent transition zone (OCT) is overprinted by early-stage magmatism, which is in good agreement with the shallow lithology measurements from IODP drilling.

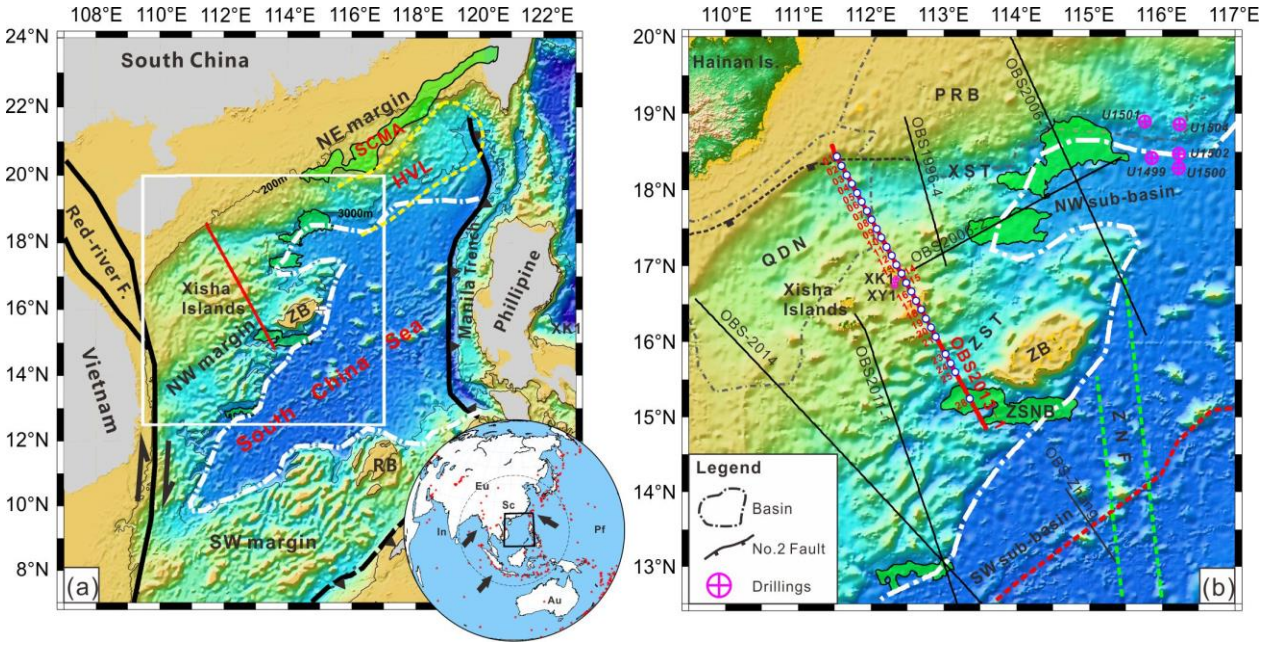

Fig. 1 Location map showing the study region in the South China Sea. (a) High magnetic anomalies close to the slopes and in the northeastern (NE) margin are both represented by green masked polygons. Distribution of the high velocity layer (HVL) is enclosed by dashed yellow line. The dashed white line is the continent-ocean boundary (COB) referring to Li and Song (2012). SCMA – South China Magnetic Anomalies along the NE margin of the SCS; RB - Reed Bank. The inset shows the tectonic setting of the SCS, in which, Eu is the Eurasia Plate, In is the India Plate, Au is the Australian Plate, Pf is the Philippine Plate and Sc is the South China block. (b) Map showing the seismic profiles and the IODP drilling sites. In which, OBS2013-1 is marked by a red line and the circles along the line represent OBS locations. Other profiles are

labeled and shown as black lines, OBS2011-1 (Huang et al., 2019); OBS-2014 (Pichot et al., 2013); OBS1996-4 (Qiu et al., 2001); OBS2006-1 (Wu et al., 2011); OBS2006-2 (Ao et al., 2012); and OBS-Zhang (Zhang et al., 2016). The dashed red line is the aborted spreading ridge. QDN - Qiongdongnan Basin; PRB - Pearl River Mouth Basin; XST - Xisha Trough; ZB – Zhongsha Bank; ZST - Zhongsha Trough; ZSNB – Zhongshanan Bain; ZNF - the Zhongnan Fracture Zone.

2 Geological Setting

The SCS margins developed along a NE-strike divergent setting due to rollback of the subducted Paleo-Pacific plate in the Late Mesozoic (Taylor and Hayes, 1983). Long-lasting continental rifting of the margins started in the latest Cretaceous to Early Paleocene (~65 Ma) and ceased prior to the progressive seafloor opening from ~32 Ma to ~15 Ma (Briais et al., 1993; Larsen et al., 2018). As a result, the SCS evolved into segmented sub-basins (Taylor and Hayes, 1983), and the margins also show along-strike deforming patterns of the continental crust (Franke et al., 2014; Hayes and Nissen, 2005). For the northern margin, the eastern segment is characterized by the presence of a high velocity layer (HVL; the location is shown in Fig. 1a) underlying either hyper-thinned continental crust or separated upper crust (McIntosh et al., 2014). A remarkable high magnetic anomaly belt in the northern margin (SCMA) has long been discussed and considered as a remnant of Mesozoic subduction arc (Wan et al., 2017). In comparison, the western section exhibits a normally extended continental crust (Hayes and Nissen, 2005), alternating with aborted rifts and rigid blocks in broad region. However, volcanic relics associated with the Mesozoic subduction have also been recognized along the northwestern and its conjugate margins, characterized by sporadically distributed high-amplitude positive magnetic anomalies (Li et al., 2018). Whether or not the HVL exists in these areas is debated, as

several wide-angle seismic surveys reported its absence (Wu et al., 2011; Qiu et al., 2001), whereas a few reflection seismic surveys and gravity modeling revealed scattered HVLs (Pichot et al., 2013; Qiu et al., 2013). Besides, performance of the ductile crustal layers also shows a high discrepancy between different investigations, in terms of the amount of stretching within the crust (Zhu et al., 2016).

The NW margin of the SCS, bordered by the Red River Fault Zone to the west (Fig. 1a), preserves lithospheric deformation features from episodes of the rifting processes. Basin analysis has revealed a zonal distribution of the tectonic stresses (Ren and Lei, 2011), including the collision-induced extrusion of the Indochina block in the west that has formed pull-apart basins like the Yingehai basin, Zhongjiannan basin and east of the Qiongdongnan Basin (Fig.1b). For the eastern part where the Xisha Islands (Paracel Islands) and the Zhongsha Trough are located, grabens and horsts were mainly shaped by normal and low-angle faults in extension and characterized by ductile shearing of the continental crust (Ren et al., 2014). Wide-angle seismic surveys have imaged highly extended continental crust with a thickness of less than 8 km along these troughs and basins, e.g., the Xisha Trough, which represents an aborted rift valley (Qiu et al., 2001). Seismic surveys using seafloor cables have identified strong post-spreading volcanism and hydrothermal activity along the rift faults, while the syn-rift igneous rocks are rarely visible above the crust (Gao et al., 2016).

Tectonic subsidence is considerably delayed for more than 10 Myrs due to ongoing rifting or rising asthenospheric material along the NW margin (Franke et al., 2014), and the uplifted basement thus provided a good place for growth of the reefs around the Xisha Islands (Ma et al., 2011). Controversy still exists mainly concerning the basement nature and age beneath the islands. Several boreholes have been drilled on the islands for dating and classifying the

basement rocks (e.g. XY1 and XK1 in Fig. 1b). Precambrian granitic rocks have been drilled and dated at the borehole XY1 (Zhang 1991). Nevertheless, results from the latest coring data from the borehole XK1 indicate that the basement rocks are constituted by Late Mesozoic igneous rocks, possibly representing the widespread volcanic intrusions over the SCS due to the Paleo-Pacific subduction (Zhu et al., 2017). Volcanic rocks dredged near the Zhongsha Bank in the east of the Xisha Islands were also dated with a Late Mesozoic age (Jin 1989). Geophysical surveys show that the Zhongsha Bank consists of extended continental crust with a thickness of more than ~20 km (Wu et al. 2011). Localized crustal deformation and magmatism was prevailing at the edge of these continental banks, as indicated by reflection seismic surveys and analog modeling on stretching machansim of the rigid blocks (Ding and Li 2016).

3 Data and Methods

3.1 Data acquisition and seismic phases

In April and May 2013, the ‘Shiptime Sharing Project of NSFC’ conducted a geophysical cruise across the Xisha Islands using the R/V ‘Shiyan 2’. During the cruise, a ~500 km long wide-angle seismic profile (OBS2013-1; Fig. 1b) striking NW-SE was acquired starting from west of the Xisha Trough and reaching the south of the Zhongsha Bank and coinciding with a multi-channel reflection seismic profile of four streamers. Thirty ocean bottom seismometers (OBS) spaced at ~15 km were deployed, among which 25 OBSs were successfully recovered and provided useful data. Four air guns with a total volume of ~98 L were deployed ~30 m behind the vessel and shot every 120 s, leading to ~300 m shot spacing at a ship speed of ~5.0 Kn.

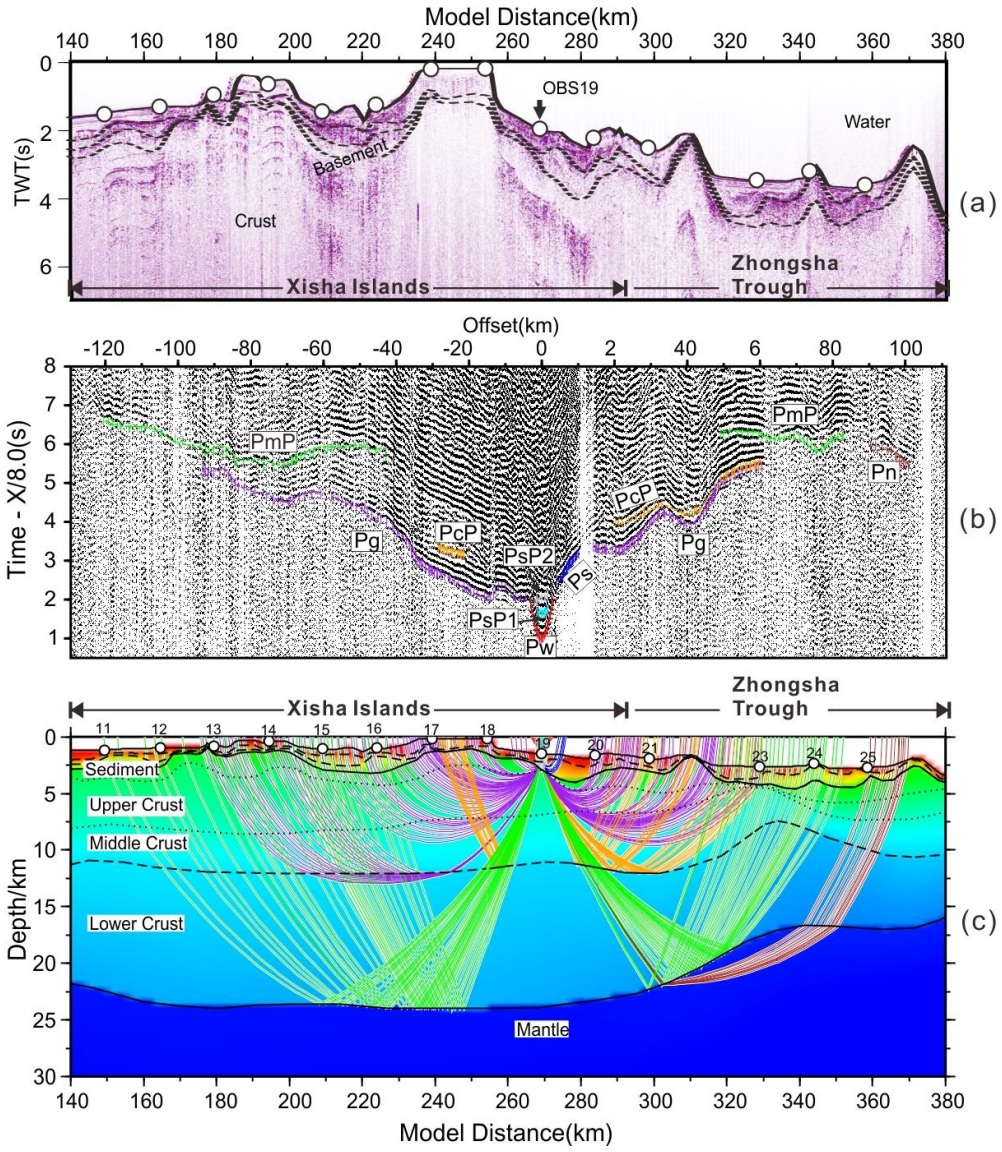

Fig. 2 Seismic modeling of the OBS data. (a) A segment of the reflection seismic data section. The white circles mark locations of the OBSs. The solid line and the dashed lines respectively represent the seafloor and the sedimentary interfaces from the forward modeling. (b) Seismic section of OBS19, overlain by the calculated travel times in different colors. The reduced velocity is 8.0 km/s. Location of OBS19 is shown in Fig.1b. (c) A segment of the forward velocity model. Seismic ray paths are shown in colored lines.

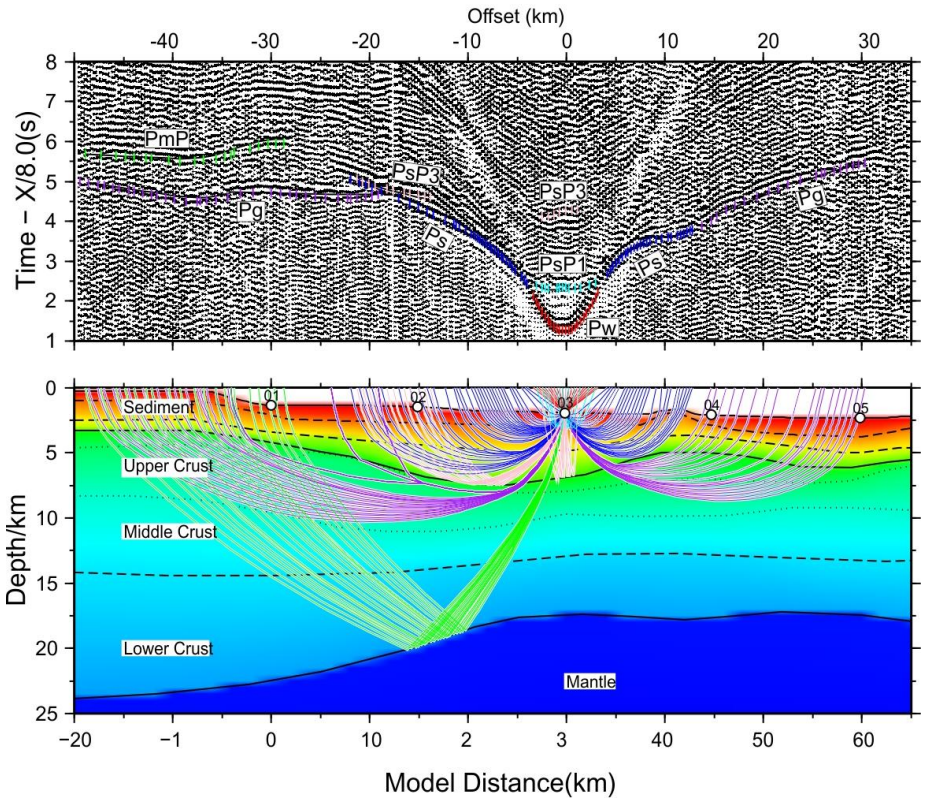

157

158 Fig. 3 Seismic modeling of the data from OBS03. The reduced velocity is 8.0 km/s. Location of
159 OBS03 is shown in Fig.1b. Seismic ray paths are shown in colored lines.

160 The raw seismic data were corrected for the clock-drift, and instrument positions were
161 relocated by fitting the direct water-wave traveltimes using the least-square method (West et al.,
162 2001). A spectrum-whitening deconvolution was used to remove the bubble reverberations and
163 highlight the primary arrivals. Automatic gain of the seismic amplitudes and zero-phase band-
164 pass filter (3-15Hz) were also applied to further enhance the seismic signals. The reflection
165 seismic data were processed following basic steps, including trace sorting, filtering and
166 automatic gain. The OBS sections show clear refracted phases traveling though the sediments
167 (Ps), the crust (Pg) and the upper mantle (Pn). Sedimentary reflections (PsP1, PsP2) as well as
168 reflections from top basement (PsP3), mid-crustal interface (PcP) and the Moho (PmP) were also

identified (Fig. 2 - 4). A total of 10346 arrivals including 5856 refractions and 3992 reflections were finally picked.

3.2 Velocity modeling

The P-wave velocity structures were constraint jointly by forward modeling (Zelt and Smith, 1992) and tomographic inversion (Korenaga et al., 2000) of the seismic data. A combination of both approaches allows drawing a user-independent velocity model including as much available information as possible (Huang et al., 2019). The forward modeling was proceeded using the layer-stripped method to decrease the misfits between the picked and calculated traveltimes (see Fig.3-4 and the supplementary material). Firstly, a 3-layer sedimentary model with variable velocities in a range of 1.7-4.5 km/s below the seafloor was constructed by forward modeling of the Ps and PsP phases. Velocities whin the sediments decide the seismic phase morphologies, which is more easily identified when the sedimentary layer is less fluctuated, as shown in the left branch of Fig.3. Velocity boundaries between the sedimentary layers as well as the basement were converted from depth to two-way traveltime and match the reflection seismic data (Fig. 2a). Secondly, tomographic inversion of the crustal structures was implemented using Pg and PmP phases, taking the sediments as input information. Finally, the inversion model was further revised by forward modeling to prevent over interpretation of the data. Velocity boundaries within the crust were continuously traced by the PcP phases (Fig. 4), thus providing information for imaging internal structures of the crust (Fig. 2). The identification and modeling of the inter-crustal interface were verified by calculating the synthetic waveforms based on zero-order asymptotic ray theory (Zelt and Ellis, 1988). Basically, the theoretical PcP phases with relative higher amplitudes correspond to the real phases that are easy to pick (Fig. 4). The velocities of the upper mantle were modeled based on the Pn phases once the crust was well constraint.

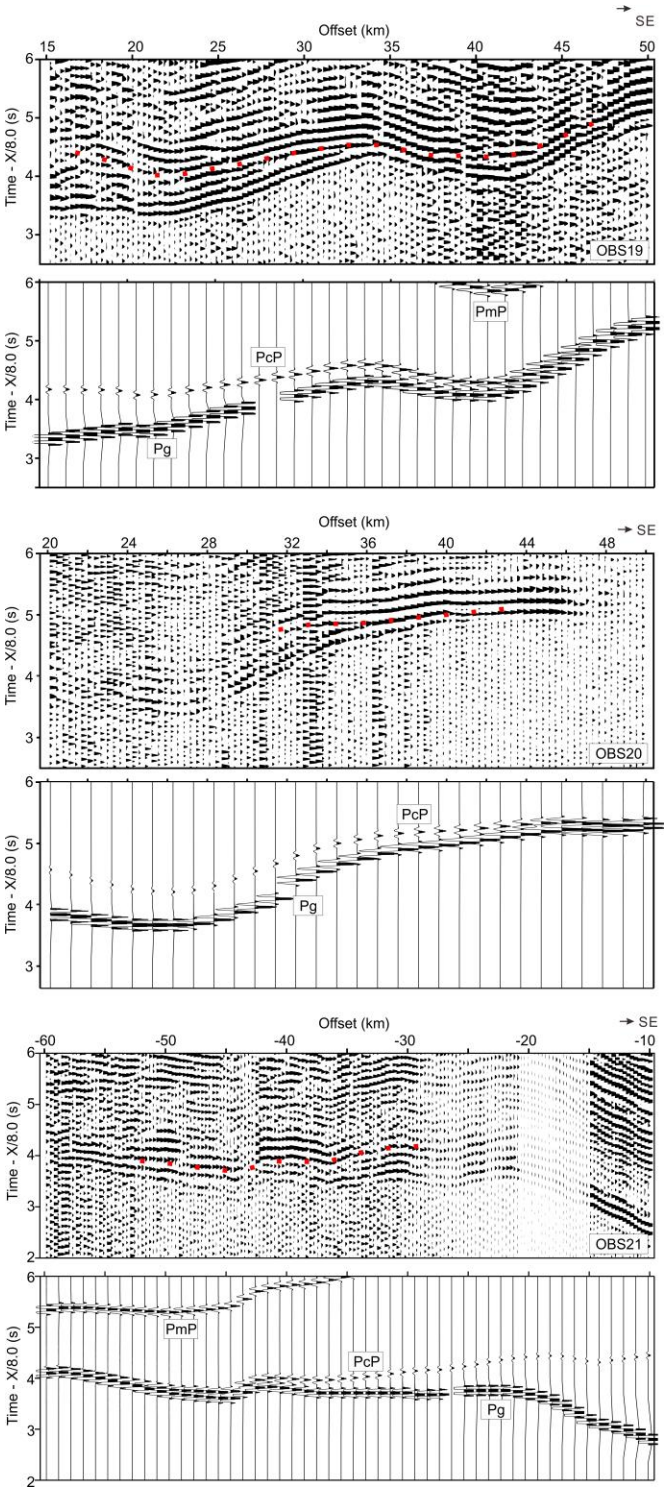

Fig. 4 The PcP phases recorded in OBS19, OBS20 and OBS21. Red dotted lines denote the picked PcP phases. For each OBS, the upper panel shows the real seismic profile, while the

lower panel shows the synthetic one based on the velocity model and the calculated traveltimes. The reduced velocity is 8.0 km/s.

4 Results

Modeling of the OBS2013-1 data resulted in a velocity model showing sedimentary and crustal structures along the complete NW margin to a depth of 30 km (Fig. 5b). The sedimentary and crustal structures will be discussed together with the interpretation of the reflection seismic data. This helps to better understand the deforming pattern of the continental crust as well as the magmatic activity along the margin. The modeling errors are discussed below, and main features of the velocity model are described according to the major tectonic units.

4.1 Error calculations of the velocity model

The tomographic model was parameterized in a grid mesh with node spacing of 0.5 km in the horizontal dimension and 0.05-0.25 km in the vertical dimension increasing downward. The Moho and the inter-crustal boundary were both defined with uniform 1 km spacing. Smoothing weighting factors for the velocity and depth were set to 200 and 20 after conducting a set of trials to avoid artifacts in the velocity models. Checkerboard tests of the model resolution were applied to the final tomographic model (Fig. 6a-c) (Korenaga et al., 2000). A rectangular perturbation pattern of 8% of the velocities, with a horizontal cell-size of 25 km and vertical cell-size 6 km can be successfully recovered (Fig. 6b and Fig. 6c). More details can be revealed in the inversion model (Fig.6d) than the forward one (Fig.5c) mainly for the upper crust, and the velocity perturbation and sizes in both models are within the identifiable range as indicated by the checkerboard tests. The uncertainty of the layered structures in the final forward model was assessed using a Monte Carlo approach (VMONTECARLO; Loureiro et al., 2016). 500,000 random models were constructed and evaluated to produce a global uncertainty map of the

velocity and depth nodes (Fig. 7). Generally, the velocity uncertainty varies between ±0.3 km/s while the Moho-depth uncertainty ranges between ±1 km. Large velocity uncertainty values were located near the Moho and the inter-crustal interface, indicating either a poor ray coverage or a strong trade-off between the depth and velocity at the velocity boundary (Loureiro et al., 2016).

4.2 Structures beneath the Xisha Trough and its flanks

A 3- to 6-km-thick Cenozoic sedimentary sequence was imaged along the west Xisha Trough, composed of three layers with velocities of 1.7-4.5 km/s and velocity discontinuities between 0.1-0.5 km/s across the interfaces. The top of the basement is characterized by a long-wavelength morphology variation across the section, showing a progressive deepening toward the shelf foot. This results in a thickened sedimentary layer and formation of a ~70 km wide half-graben. A basement high is located at the trough center and overlain by a seamount with average seismic velocity of ~3.5 km/s. For comparison, the sedimentary cover of the Xisha Islands is much thinner (~2.5 km) and overlies a relative shallow basement at ~3 km depth.

The Moho is located deeper than 22 km below the shelf at the Xisha Islands, and rises progressively toward the Xisha Trough to ~17.5 km. The P-wave velocity increases from 5.0 km/s at the basement's top to ~6.8 km/s at the bottom of the crust. A velocity boundary near the isovelocity contour of 6.4 km/s was sampled by the PcP phases in a 30-km wide area, and the velocity contrast across this boundary is ~0.1 km/s.

4.3 Zhongsha Trough and Zhongshanan Basin

A series of horsts and grabens developed across the Zhongsha Trough, with basement highs and intermediately thick sedimentary deposits (~3 km). Velocities at the basement top vary between 5.0 and 5.6 km/s. The Moho becomes shallower rapidly from ~23 km in the Xisha

Islands to ~15 km and ~11 km respectively in the Zhongsha Trough and the Zhongshanan Basin, over a distance of ~100 km. The crustal thickness is ~6 km in the Zhongshanan Basin, where a lens-shaped layer less than 2 km thick was modeled by seismic velocities of ~3.8 km/s on top of the basement. It was also identified in the reflection seismic section and corresponds to a high positive magnetic anomaly (~170 nT; Fig. 5a and Fig. 9c).

The crustal velocities also show a complex variation across the Zhongsha Trough. The upper crust, taking the 6.4 km/s isovelocity line as the lower boundary, is stretched to be less than 5 km thick and accompanied by uplifted lower crust. Accordingly, velocity in the lower crust increases by ~0.3 km/s forming a sharp velocity contrast across the boundary (Fig.5c-d), which can be continuously traced in a range of ~90 km by the PcP phases (Fig. 4). A similar inter-crustal velocity boundary is located beneath the Zhongshanan Basin, where the velocity contrast is slightly reduced to 0.1-0.2 km/s (Fig.5c-d). The uppermost mantle beneath the basin shows a lower average velocity at ~7.7 km/s than the adjacent areas, in a horizontal range of ~50 km and vertical depth of more than 3 km from the Moho.

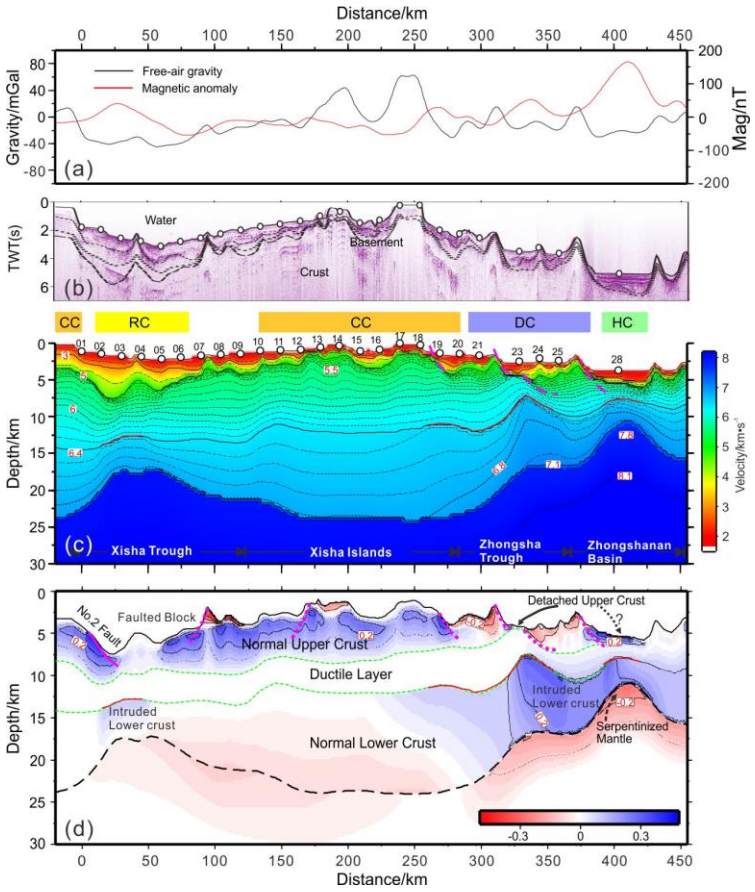

Fig. 5 Final seismic model and velocity perturbation of the OBS2013-1. (a) Gravity anomaly (black line) and magnetic anomaly (red line). (b) Reflection seismic data section. (c) P-wave velocity model. CC - continental crust; RC - rift valley crust; DC - detached crust; HC - hyper-thinned crust. (d) Velocity perturbation in the crust shown in positive (blue) and negative (red) values. The thick red lines show the faults cutting the basement. The green lines outline the ductile layer between the normal upper crust and the lower crust. The black dashed line shows the Moho, while the thin red solid lines show the constraint inter-crustal interface.

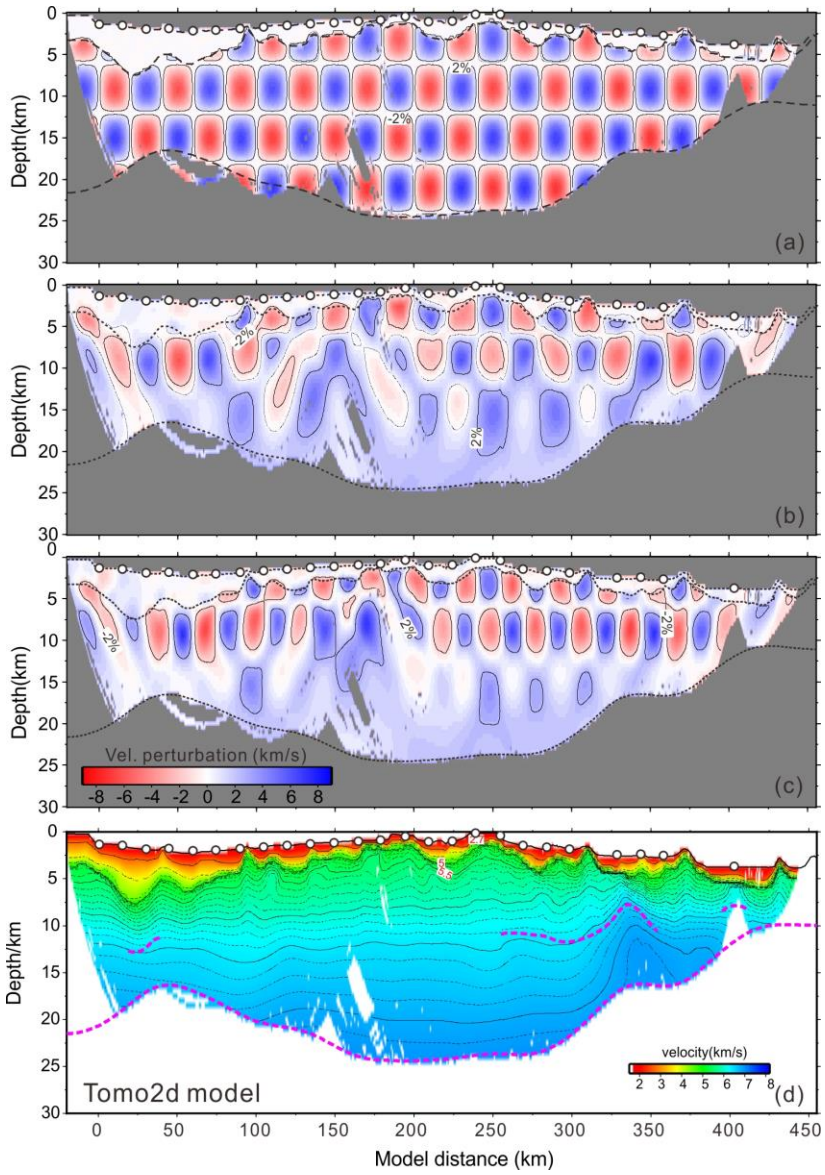

Fig. 6 Results of the checkerboard tests for the velocity model. The amplitude of the velocity perturbation is 8%. (a) Original perturbed forward model, with anomaly size in 25 km × 6 km. (b) Recovered anomalies in 25 km × 6 km. (c) Recovered anomalies in 15 km × 6 km. (d) The tomographic inversion model. In which, the purple dashed lines are the inverted velocity interfaces.

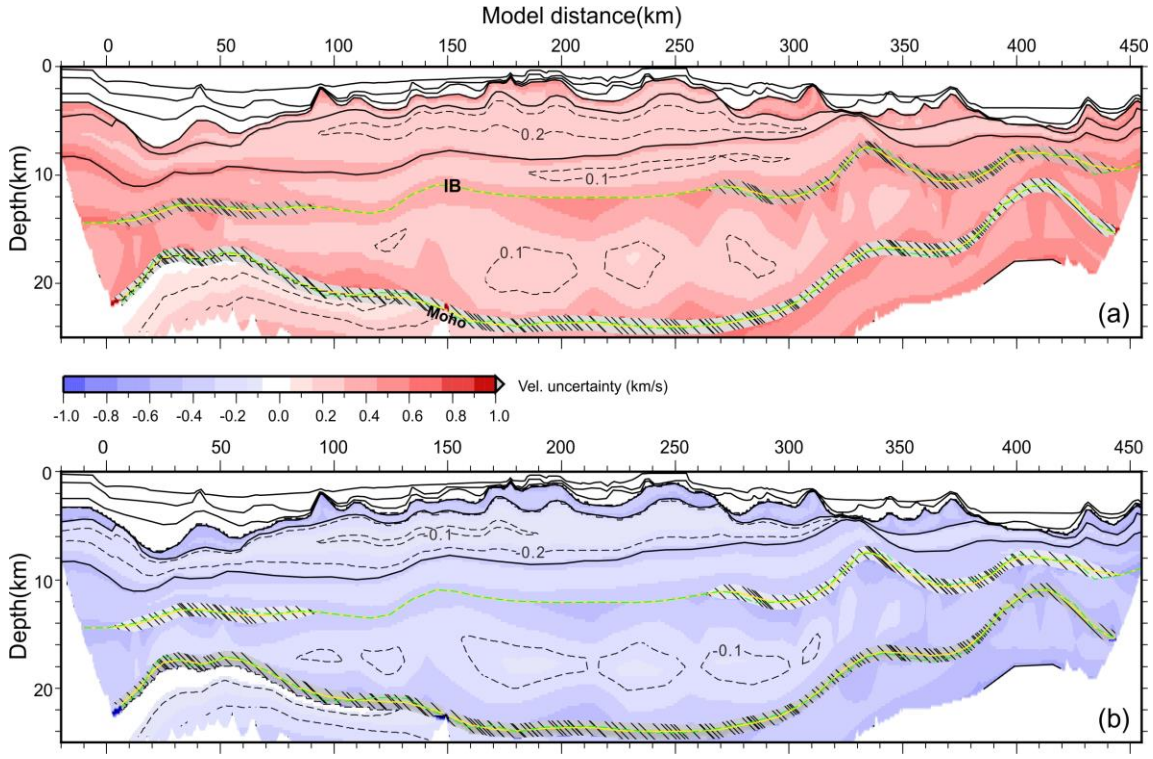

Fig. 7 Monte Carlo uncertainty tests of the forward model. The hatched areas at the intra-crustal boundary (IB) and the Moho denoted the depth uncertainties for the both boundaries. Dashed yellow and green lines, respectively, indicate the best random model's and the forward model's IB and Moho. (a) Positive velocity uncertainties of the forward model. (b) Negative velocity uncertainties.

5 Discussion

5.1 Intracrustal deformation and identification of a ductile layer

The velocity model provides direct evidence for the intracrustal deformation, as the inter-crustal boundary (Fig. 7a) and the Moho have been precisely mapped. The model can be divided into four distinct sections according to these crustal structures (Fig. 5c). The Xisha Islands and the shelf area are identified as continental blocks that have experienced weak and uniform stretching. The crustal thickness (~22 km) is in good agreement with the values derived from the

281 receiver functions on the islands (Huang et al., 2011). Along the western Xisha Trough, the crust
282 has been stretched to be as thin as ~10 km beneath the half graben that is named the Songnan
283 Sag of the Qiongdongnan Basin (Ren et al., 2014). Between OBS01 and OBS02, the top
284 basement shows an increased velocity by ~0.5 km/s compared to both sides (Fig. 5d), which is
285 also proposed by Qiu et al. (2013). In earlier work, it was proposed to represent a detachment
286 fault that shaped the half graben within the basin (Ren et al. 2014). This fault may not only
287 contribute to the gravity anomaly identified along our model (Fig. 5a), but also the associated
288 variation of the seismic velocity (Fig. 5d). A similar complex basement shape was also presented
289 by Qiu et al. (2001), and the basement high in the center can be interpreted as a rotated
290 continental block related to a rollover anticline (Ren et al., 2014). Using an initial crustal
291 thickness of 30 km, it corresponds to a stretching factor β of 3.0 that is less than the value
292 calculated from the Xisha Trough (β=~3.8; Qiu et al., 2001), probably due to the westwards
293 propagated continental rifting.

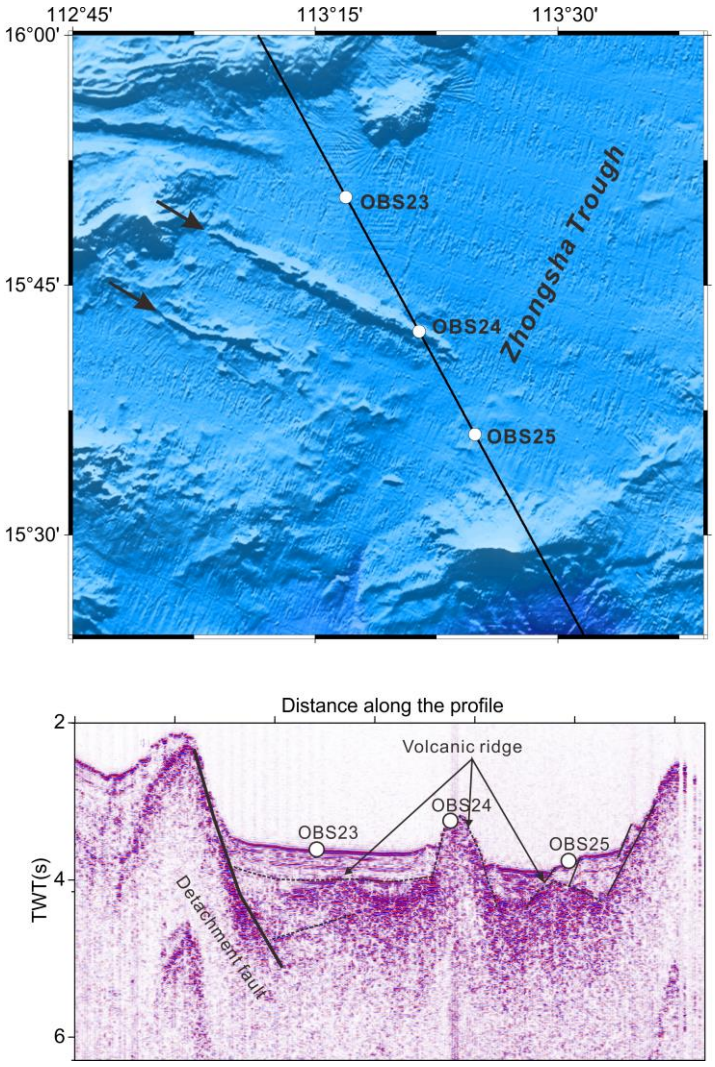

Fig. 8 Enlarged topography of the Zhongsha Trough (top), where the white circles are OBSs and the two arrows show the volcanic ridges. (Bottom): reflection image of the volcanic ridges/intrusion.

In the southern part of the profile, a prominent rise of the Moho and a relatively shallower basement than the north are modeled, reflecting the delayed subsidence of the NW margin of the SCS (Franke et al., 2014). Instead of a wide rift valley like the Xisha Trough, a series of half grabens distributed along this region bordered by seaward dipping faults and corresponding basement highs were imaged. These faults extend down to depths of approximately 7 km where

the velocity shows high perturbations and distinctive gradients (Fig. 5c and Fig. 5d). Strikingly, the crust with velocity lower than 6.0 km/s is dismantled along a small window about 20 km wide in the Zhongsha Trough (near OBS23), with rotated basement on both flanks that might also represent rollover structures. Magnetic profiles show anomalies of ~50 nT along the Zhongsha Trough (Fig. 5a), following closely these faults and rollover structures. In contrary to the SCMA, this weak-to-intermediate anomaly might correspond to metamorphic basements or fault-controlled volcanic ridges as shown in the topography (Fig. 8).

The top boundary of the lower crust can be imaged in an extended range, buried at a depth of ~13 km across the Zhongsha Trough (Fig. 5c). Previous long-cable seismic surveys also imaged reflectors at around ~15 km depth in the northern and western SCS margins, where the listric faults sole out and which may represent the brittle-ductile transition zone (Lester et al., 2014). By considering the brittlely deformed upper crust along the detachment fault, we propose that a ~5 km thick ductile layer exists beneath the upper crust, separated from the lower crust by a shearing surface (Fig. 5c-d). Reflected phases from the top boundary of this ductile layer were not detected, possible due to a small seismic impedance contrast or a low resolution of the OBS data. Franke et al. (2014) suggested that the ductile layer might be the shallower portion of the lower crust, which is important for compensating the upper crustal extension. Shi et al. (2002) have also presented a similar rheological stratification across the Xisha Trough based on the thermal modeling, in which the lower crust shows high rheological weakness. Thickness of the lower crust beneath the shearing surface appears to be 2-3 km more under the Zhongsha Trough than the blocks on both sides (Fig. 5c). The bottom of the lower crust shows slightly increased velocities of up to 7.1 km/s (Fig. 5c-d). Similar to the Kenya and Baikal rifts, this may indicate magmatic additions during rifting (Thybo and Nielsen, 2009). From our model, the highly

reflective top of the lower crust indicates a prominent velocity/density contrast, which could have been enhanced by a front of intruded sills blocked at the ductile boundary (Fig. 5d and Fig. 10c, d). Nevertheless, the average velocity of the lower crust of ~6.8 km/s is much lower than the HVL (possibly corresponding to volcanic underplating) in the NE margin (Wan et al., 2017), reflecting different extents or sources of the volcanic activities.

5.2 Hyper-thinned continental crust in the OCT

A stretching factor of ~5 can be calculated in the Zhongshanan Basin off Zhongsha Bank, representing a possible location for breakup of the continental crust (White and McKenzie, 1989). In order to determine the nature of the crust, averaged velocity-depth profiles were extracted from the velocity model (Fig. 9b). It shows that the crustal velocities and thickness are in good agreement with those from typical Atlantic oceanic crust (White et al., 1992). A two-layer structure, separated by a clear velocity step, represents the oceanic layer 2 and layer 3. However, the magnetic anomaly in this area does not show the pattern with clear stripes as found in the deep basin representing the steadily formed oceanic crust (Fig. 9a). Such long-wavelength magnetic anomalies can also be recognized alongside other slope regions of the SCS (Fig. 9a). Here, the buried layer (velocity of 3.8 km/s) overlying the basement may represent volcanic extrusions and contribute partly to the magnetic anomaly. In addition, the horizontally overlying strata indicate that these magmatic activities occurred earlier (Fig. 9c). A similar magnetic anomaly has been observed along the OCT of the Central and North Atlantic margins, representing pre-spreading magmatic intrusions or underplating (Nirrengarten et al., 2017). However, normal crustal velocities (5.0-7.0 km/s) and a reflective Moho in our model exclude both underplated melting and exhumed mantle as an explanation for these anomalies. More

likely, the faults at the rim of blocks, as well as the igneous intrusion suggest a hyper-thinned continental crust in this region.

We also compiled the crustal structures along the slope regions with high magnetic anomaly in the NW margin and the oceanic basins from published velocity models (Fig. 9b) (Huang et al., 2011; Wu et al., 2011; Zhang et al., 2016; Zhao et al., 2018). The structures share common characteristics including a narrow high velocity band and a high velocity gradient of the upper crust similar to the global characteristics of the OCT (Christensen and Mooney, 1995). Variation of the crustal thicknesses (6-9 km) can be explained by extents of magmatic additions or influences from pre-rifting structures. In contrast, the normal oceanic crust is relatively thin, about 5 to 8 km. The seismic velocity and gradient of layer 2 in the spreading ridge (C5e-C5c) decreased rapidly compared to that near the OCT region (C12-C11) (Fig.9b), reflecting a greater degree of fracturing and less compaction of the cracks (White et al., 1992). At the same time, there are similar velocity differences between the OCT and the NW Sub-basin with the oldest oceanic crust (Fig. 9a, b). The narrow OCT (~50 km), as well as the volcanic intrusions and extrusions suggest a prominent magmatism at late-stage rifting, which may lead to a rapid onset of the embryonic oceanic crust mixed with the highly fractured continental crust (Fig. 10c-d). The results are consistent with the IODP drilling that revealed a narrow and fast rift-to-drift transition with abundant MORB-type melts along the margin of the NW Sub-basin (Larsen et al., 2018).

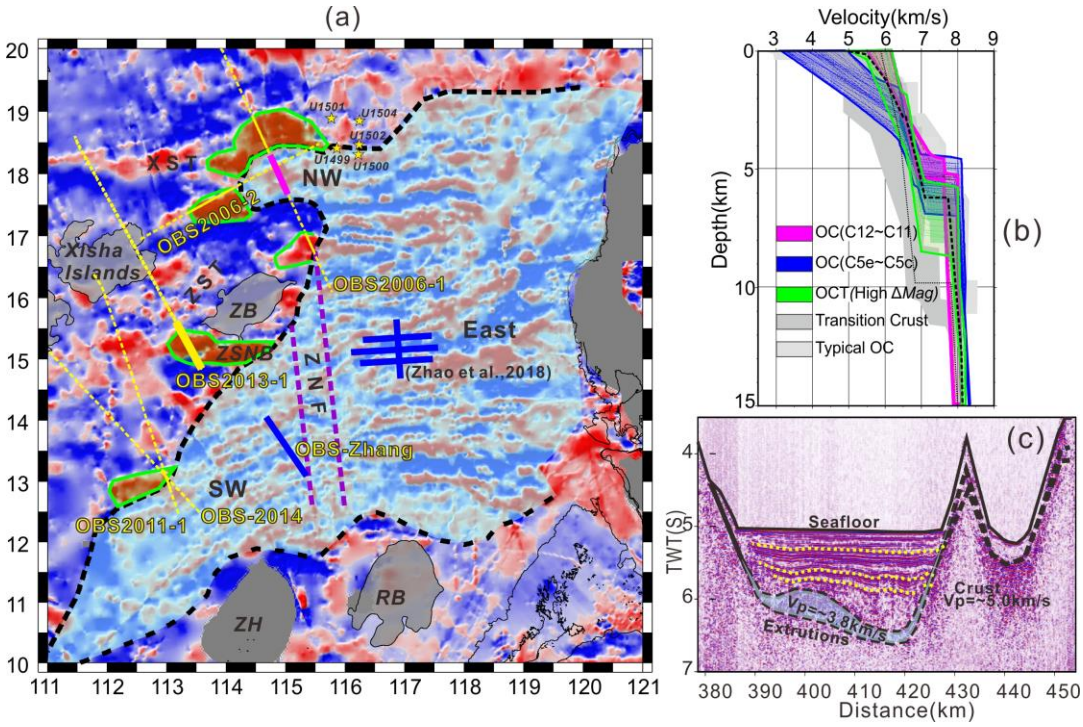

Fig. 9 (a) Magnetic anomaly map of the SCS. Dashed yellow lines denote OBS profiles along the NW margin, while solid blue lines denote the ones at the spreading ridge. The solid purple line denotes a segment of the OBS2006-1 in the NW Sub-basin. Green lines enclose high magnetic anomalies near the slopes. Yellow stars are IODP drillings during the 367/368 cruises. NW - Northwestern Sub-basin; East - Eastern Sub-basin; SW - Southwestern Sub-basin; RB - Reed Bank; XST – Xisha Trough; ZB – Zhongsha Bank; ZST – Zhongsha Trough; ZH - Zhenghe Massif; ZSNB – Zhongshanan Basin. (b) Compilation of the velocity structures in the SCS. The dashed line represents the averaged velocity-depth profile in the Zhongshanan basin. OC – Oceanic crust. (c) A segment of the reflection seismic profile along the OBS2013-1, which is denoted by the bold solid yellow line in Fig.9a. The yellow dotted lines denote the sedimentary boundaries, and the transparent shaded area denotes the buried volcanic extrusions.

5.3 Origin of the low-velocity upper mantle and the high magnetic anomaly

The obvious low-velocity structure (~7.7 km/s; Fig. 5b-c) extending more than 3 km below the Moho in the Zhongjiannan Basin can be interpreted as an indicator of serpentinization in the upper mantle (Miller and Christensen, 1997) or the presence of partial melting (Henry et al., 1990). The ~3 km thick molten material with velocity of ~7.7 km/s would require a Moho temperature greater than 1000 °C (White and Mckenzie, 1989). However, the heat flow value measured here is about 60 mW/m^2 (Shi et al., 2002), which roughly means that the temperature below the crust is less than 500 °C, not high enough to cause present-day melting. Since the crust is only ~6 km thick, serpentinization could be originating from penetration of water into the upper mantle along the normal faults bordering the blocks (Fig. 10c) (Dean et al., 2000). In this scenario, seismic velocity of ~7.7 km/s corresponds to about 13% of the partial serpentinization of the upper mantle (Mechie et al., 1994). A similar serpentinized mantle has been proposed to exist (7.6 km/s in velocity and ~3 km in thickness) beneath the fossil spreading ridge in the Southwest Sub-basin (OBS-Zhang; Fig. 1b) (Zhang et al., 2016). There, an extremely low heat flow < 50 mW/m^2 was measured (He et al., 2001) and was considered to be related to the Zhongnan Fracture Zone (the ZNF in Fig. 1b). In any case, the limited extend of serpentinized mantle may indicate a short-term fault activity (Bayrakci et al., 2016) or oblique extension (White et al., 1992). This agrees again with the narrow OCT in the study region due to the rapid onset of the oceanic crust accretion.

Spectral analysis on the magnetic field in the SCS indicates that deep magnetic layers at the lower crust or upper mantle contribute to both the SCMA and anomalies near the OCT (Li and Song, 2012). The mantle serpentinization of ~13% beneath the Zhongshanan Basin, if it exists, should not be the dominant source of the high magnetic anomaly in this area, as very partially serpentinized upper mantle contributes only little to the magnetic anomaly (Fujii et al., 2016).

The long-wavelength magnetic anomalies were frequently observed over cratons and forearcs and were considered to be caused by magnetic uppermost mantle (Ferre et al., 2014). Forward modeling of the magnetic anomalies from xenoliths show that high magnetization of the upper mantle usually corresponds to low geothermal settings (Friedman et al., 2014). Normally, rift valleys such as the Zhongsha Trough might be too hot to form strong mantle magnetism, which is verified by the magnetic data in the northwestern margin (Fig.9a). However, the heat flow values are commonly low along the Zhongjiannan Basin, which may be related to the highly fractured crust. The deep mantle magma accompanying the formation of the embryonic oceanic crust could have provided material source for the mantle magnetite.

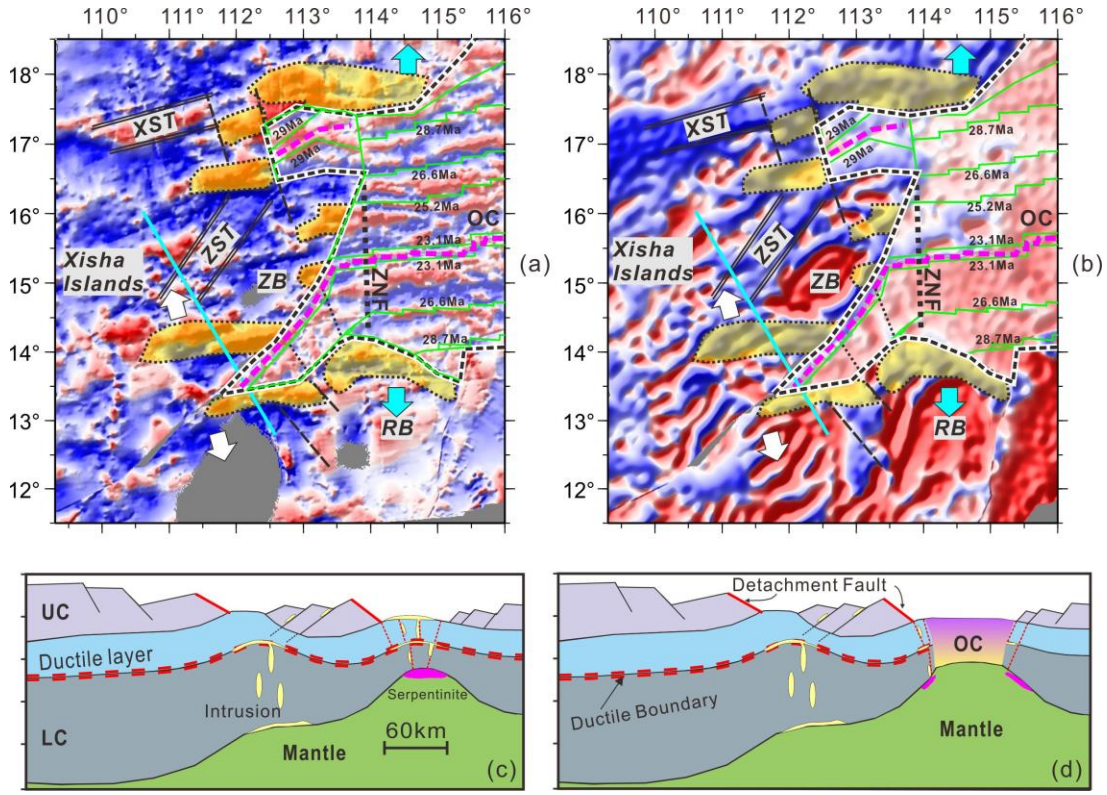

Fig. 10 Maps of the magnetic (a) and gravity anomaly (b) of the SCS reconstructed at 22.5 Ma using rotation poles from the Gplates software (Boyden et al., 2011). Yellow areas mask the high magnetic anomaly representing the OCT along the slopes. Green lines are identified magnetic

anomalies, representing mature oceanic crust. The blue and white arrows represent the early and late stages of the seafloor spreading (Briais et al., 1993), respectively. Thin dashed lines represent the possible transform faults identified based on the gravity and magnetic anomalies. Bold dashed lines denote the reconstructed COB. (c, d): Schematic models for the evolution of the continental margin before (c) and after (d) the seafloor spreading between the Zhongsha Bank (ZB) and the Reed Bank (RB). The location is shown by the blue lines in Fig. 10a and Fig. 10b. UC - upper crust; LC - lower crust; OC - Oceanic crust.

6 Conclusions

Precisely reflection and wide-angle seismic modeling revealed the crustal structures in the NW margin of the SCS. The conclusions are as following: 1) Crustal deformation was controlled by detachment faults that sole out into a ductile layer at depths of ~7 km below the basement. A sharp velocity boundary exists between this ductile layer and the lower crust in the Zhongsha Trough. 2) The brittle upper crust has been detached along a ~20 km wide zone in the Zhongsha Trough, accompanied by thickened lower crust due to magmatic additions. 3) A highly thinned continental crust (~6 km thick) in the Zhongshanan Basin represents the OCT where high magnetic anomaly is related to magmatic addition and upper mantle magnetism. Below the crust, the upper mantle was likely to be partially serpentinized due to short-term fault activity shortly before the oceanic spreading. 4) Prominent magmatism at late-stage rifting penetrated the OCT and may lead to a rapid onset of the embryonic oceanic crust.

Acknowledgments

The NSFC Open Research Cruise (NORC2013-08), funded by the Shiptime Sharing Project of NSFC, has supported the data acquisition of this work. This cruise was conducted onboard R/V “Shiyan 2” by the scientific team and the crew. This study was supported by National Key R&D

Program of China [grant number: 2018YFC0309800] and National Natural Science Foundation of China [grant numbers: 41676045, 41674092 and 41306046]. The GMT software (Wessel and Smith, 1995) and Seismic Unix software package (Stockwell, 1999) were used to plot the figures. We thank Stephane Operto for providing codes packages of filtering and deconvolution of OBS data. We also thank Dieter Franke for his constructive comments on the discussion. Datasets for this research are available at the link http://doi.org/10.5281/zenodo.3677587.

References

1. Ao, W., Zhao, M.H., Qiu, X.L., Ruan, A.G., Li, J.B., 2012. Crustal structure of the Northwest Sub-Basin of the South China Sea and its tectonic implication. Earth Science - Journal of China University of Geosciences (in Chinese) 37, 779-790.
2. Bayrakci, G., Minshull, T.A., Sawyer, D.S., Reston, T.J., Klaeschen, D., Papenberg, C., Ranero, C., Bull, J.M., Davy, R.G., Shillington, D.J., Perez-Gussinye, M., Morgan, J.K., 2016. Fault-controlled hydration of the upper mantle during continental rifting. Nat Geosci 9, 384-388.
3. Boyden, J.A., Müller, R.D., Gurnis, M., Torsvik, T.H., Clark, J.A., Turner, M., Ivey-Law, H., Watson, R.J., Cannon, J.S., 2011. Next-generation plate-tectonic reconstructions using GPlates. Geoinformatics Cyber infrastructure for the Solid Earth Sciences, 95-114.
4. Briais, A., Partriat, P., Tapponnier, P., 1993. Updated interpretation of magnetic anomalies and seafloor spreading in the South China Sea: Implications for the Tertiary Tectonics of Southeast Asia. J Geophys Res 98, 6299-6328.
5. Brune, S., Heine, C., Perez-Gussinye, M., Sobolev, S.V., 2014. Rift migration explains continental margin asymmetry and crustal hyper-extension. Nat Commun 5, doi: 10.1038/ ncomms5014.

462 6. Christensen, N.I., Mooney, W.D., 1995. Seismic Velocity Structure and Composition of the
463 Continental-Crust - a Global View. J Geophys Res-Sol Ea 100, 9761-9788.
464 7. Dean, S.M., Minshull, T.A., Whitmarsh, R.B., Louden, K.E., 2000. Deep structure of the
465 ocean-continent transition in the southern Iberia Abyssal Plain from seismic refraction
466 profiles: The IAM-9 transect at 40 degrees 20 ' N. J Geophys Res-Sol Ea 105, 5859-5885.
467 8. Ding, W.W., Li, J.B., 2016. Propagated rifting in the Southwest Sub-basin, South China Sea:
468 Insights from analogue modelling. J Geodyn, 100, 71-86.
469 9. Ferre, E.C., Friedman, S.A., Martin-Hermandez, F., Feinberg, J.M., Till, J.L., lonov, D.A.,
470 Conder, J.Z., 2014. Eight good reasons why the uppermost mantle could be magnetic.
471 Tectonophysics 624, 3-14.
472 10. Franke, D., Savva, D., Pubellier, M., Steuer, S., Mouly, B., Auxietre, J.L., Meresse, F.,
473 Chamot-Rooke, N., 2014. The final rifting evolution in the South China Sea. Mar Petrol
474 Geol 58, 704-720.
475 11. Friedman, S.A., Feinberg, J.M., Ferre, E.C., Demory, F., Martin-Hernandez, F., Conder, J.A.,
476 Rochette, P., 2014. Craton vs. rift uppermost mantle contributions to magnetic anomalies in
477 the United states interior. Tectonophysics 624, 15-23.
478 12. Fujii, M., Okino, K., Sato, H., Nakamura, K., Sato, T., Yamazaki, T., 2016. Variation in
479 magnetic properties of serpentinized peridotites exposed on the Yokoniwa Rise, Central
480 Indian Ridge: Insights into the role of magnetite in serpentinization. Geochem Geophy
481 Geosy 17, 5024-5035.
482 13. Gao, J.W., Wu, S.G., McIntosh, K., Mi, L.J., Liu, Z., Spence, G., 2016. Crustal structure and
483 extension mode in the northwestern margin of the South China Sea. Geochem Geophy
484 Geosy 17, 2143-2167.

14. Hayes, D.E., Nissen, S.S., 2005. The South China Sea margins: Implications for rifting contrasts. Earth Planet Sc Lett 237, 601-616.
15. He, L.J., Wang, K.L., Xiong, L.P., Wang, J.Y., 2001. Heat flow and thermal history of the South China Sea. Phys Earth Planet In 126, 211-220.
16. Henry, W.J., Mechie, J., Maguire, P.K.H., Khan, M.A., Prodehl, C., Keller, G.R., Patel, J., 1990. A Seismic Investigation of the Kenya Rift-Valley. Geophysical Journal International 100, 107-130.
17. Huang, H.B., Qiu, X.L., Xu, H.L., Zhao, M.H., Hao, T.Y., Xu, Y., Li, J.B., 2011. Preliminary results of the earthquake observation and the onshore offshore seismic experiments on Xisha Block. Chinese J. Geophys. (in Chinese) 54, 3161-3170.
18. Huang, H.B., Qiu, X.L., Pichot, T., Klingelhoefer., F., Zhao, M.H., Wang, P., Hao, T.Y., 2019. Seismic structure of the northwestern margin of the South China Sea: implication for asymmetric continental extension. Geophys. J. Int. 218, 1246-1261.
19. Huismans, R.S., Beaumont, C., 2014. Rifted continental margins: The case for depth-dependent extension. Earth Planet Sc Lett 407, 148-162.
20. Jian, Z.M., Larsen, H.C., and Alvarez Zarikian, C.A., and the Expedition 368 Scientists, 2018. Expedition 368 preliminary report: South China Sea rifted margin: International Ocean Discovery Program. doi: 10.14379/iodp.pr.368.2018
21. Jin, X.L., 1989. The geosciences research report in South China Sea. Donghai Mar. Sci., (in Chinese) 7, 30-42.
22. Korenaga, J., Holbrook, W.S., Kent, G.M., Kelemen, P.B., Detrick, R.S., Larsen, H.C., Hopper, J.R., Dahl-Jensen, T., 2000. Crustal structure of the Southeast Greenland margin

from joint refraction and reflection seismic tomography. Journal of Geophysical Research Atmospheres 105, 21591-21614.

23. Larsen, H.C., Mohn, G., Nirrengarten, M., Sun, Z., Stock, J., Jian, Z., Klaus, A., Alvarez-Zarikian, C.A., Boaga, J., Bowden, S.A., Briais, A., Chen, Y., Cukur, D., Dadd, K., Ding, W., Dorais, M., Ferré, E.C., Ferreira, F., Furusawa, A., Gewecke, A., Hinojosa, J., Höfig, T.W., Hsiung, K.H., Huang, B., Huang, E., Huang, X.L., Jiang, S., Jin, H., Johnson, B.G., Kurzawski, R.M., Lei, C., Li, B., Li, L., Li, Y., Lin, J., Liu, C., Liu, C., Liu, Z., Luna, A.J., Lupi, C., McCarthy, A., Ningthoujam, L., Osono, N., Peate, D.W., Persaud, P., Qiu, N., Robinson, C., Satolli, S., Sauermilch, I., Schindlbeck, J.C., Skinner, S., Straub, S., Su, X., Su, C., Tian, L., van der Zwan, F.M., Wan, S., Wu, H., Xiang, R., Yadav, R., Yi, L., Yu, P.S., Zhang, C., Zhang, J., Zhang, Y., Zhao, N., Zhong, G., Zhong, L., 2018. Rapid transition from continental breakup to igneous oceanic crust in the South China Sea. Nat Geosci 11, 782-789.
24. Lester, R., Van Avendonk, H.J.A., McIntosh, K., Lavier, L., Liu, C.S., Wang, T.K., Wu, F., 2014. Rifting and magmatism in the northeastern South China Sea from wide-angle tomography and seismic reflection imaging. J Geophys Res-Sol Ea 119, 2305-2323.
25. Li, C.F., Song, T.R., 2012. Magnetic recording of the Cenozoic oceanic crustal accretion and evolution of the South China Sea basin. Chin Sci Bull 57, 3165-3181.
26. Li, F.C., Sun, Z., Yang, H.F., 2018. Possible spatial distribution of the Mesozoic volcanic arc in the present-day South China Sea continental margin and its tectonic implications. J Geophys Res-Sol Ea 123, 6215-6235.

27. Loureiro, A., Afilhado, A., Matias, L., Moulin, M., Aslanian, D., 2016. Monte Carlo approach to assess the uncertainty of wide-angle layered models: Application to the Santos Basin, Brazil. Tectonophysics 683, 286-307.
28. Ma, Y.B., Wu, S.G., Lv, F.L., Dong, D.D., Sun, Q.L., Lu, Y.T., Gu, M.F., 2011. Seismic characteristics and development of the Xisha carbonate platforms, northern margin of the South China Sea. J Asian Earth Sci 40, 770-783.
29. McIntosh, K., Lavier, L., van Avendonk, H., Lester, R., Eakin, D., Liu, C.S., 2014. Crustal structure and inferred rifting processes in the northeast South China Sea. Mar Petrol Geol 58, 612-626.
30. Mechie, J., Fuchs, K., Altherr, R., 1994. The Relationship between Seismic Velocity, Mineral-Composition and Temperature and Pressure in the Upper-Mantle - with an Application to the Kenya Rift and Its Eastern Flank. Tectonophysics 236, 453-464.
31. Miller, D.J., Christensen, N.I., 1997. Seismic velocities of lower crustal and upper mantle rocks from the slow spreading Mid-Atlantic Ridge, south of the Kane transform zone (MARK). Proceedings of the Ocean Drilling Program Scientific Results 25, 763-771.
32. Nirrengarten, M., Manatschal, G., Tugend, J., Kusznir, N.J., Sauter, D., 2017. Nature and origin of the J-magnetic anomaly offshore Iberia-Newfoundland: implications for plate reconstructions. Terra Nova 29, 20-28.
33. Pichot, T., Delescluse, M., Chamot-Rooke, N., Pubellier, M., Qiu, Y., Meresse, F., 2013. Deep crustal structure of the conjugate margins of the SW South China Sea from wide-angle refraction seismic data. Mar Petrol Geol 2013, 1-17.

549 34. Qiu, N., Wang, Z.F., Xie, H., Sun, Z.P., Wang, Z.W., Sun, Z., Zhou, D., 2013. Geophysical
550 investigations of crust-scale structural model of the Qiongdongnan Basin, Northern South
551 China Sea. Marine Geophysical Research 34, 259-279.
552 35. Qiu, X.L., Ye, S.Y., Wu, S.M., Shi, X.B., Zhou, D., Xia, K.Y., Flueh, E.R., 2001. Crustal
553 structure across the Xisha Trough, northwestern South China Sea. Tectonophysics 341, 179-
554 193.
555 36. Ren, J.Y., Lei, C., 2011. Tectonic stratigraphic framework of Yinggehai-Qiongdongnan
556 Basins and its implication for tectonic province division in South China Sea. Chinese J.
557 Geophys. (in Chinese) 54, 3303-3314.
558 37. Ren, J.Y., Zhang, D.J., Tong, D.J., Huang, A.M., Wang, Y.H., Lei, C., Zuo, Q.M., Zhao,
559 Y.H., He, W.J., Yang, L.L., 2014. Characterizing the nature, evolution and origin of
560 detachment fault in central depression belt, Qiongdongnan Basin of South China Sea:
561 evidence from seismic reflection data. Acta Oceanol Sin 33, 118-126.
562 38. Shi, X.B., Zhou, D., Qiu, X.L., Zhang, Y.X., 2002. Thermal and rheological structures of the
563 Xisha Trough, South China Sea. Tectonophysics 351, 285-300.
564 39. Stockwell, J.W., 1999. The CWP/SU: seismic Un*x package, Comput. Geosci., 25, 415-419.
565 40. Sun, Z., Stock, J., and Klaus, A., and the Expedition 367 Scientists, 2018. Expedition 367
566 preliminary report: South China Sea rifted margin: International Ocean Discovery Program.
567 doi: 10.14379/iodp.pr.367.2018
568 41. Taylor, B., Hayes, D.E., 1983. Origin and history of the South China Sea basin, in: Hayes,
569 D.E. (Ed.), The tectonic and geologic evolution of Southeast Asia Seas and Islands.
570 Geophysical Monograph, Washington, pp. 23-56.

42. Thybo, H., Nielsen, C.A., 2009. Magma-compensated crustal thinning in continental rift zones. Nature 457, 873-876.
43. Wan, K.Y., Xia, S.H., Cao, J.H., Sun, J.L., Xu, H.L., 2017. Deep seismic structure of the northeastern South China Sea: Origin of a high-velocity layer in the lower crust. J Geophys Res-Sol Ea 122, 2831-2858.
44. Wessel, P., Smith, W.H., 1995. New version of the generic mapping tools, EOS, Trans. Am. Geophys. Un., 76, 329.
45. West, M., Menke, W., Tolstoy, M., Webb, S., Sohn, R., 2001. Magma storage beneath axial volcano on the Juan de Fuca mid-ocean ridge. Nature, 413, 833-836.
46. White, R., McKenzie, D., 1989. Magmatism at Rift Zones - the Generation of Volcanic Continental Margins and Flood Basalts. J Geophys Res-Solid 94, 7685-7729.
47. White, R.S., McKenzie, D., Onions, R.K., 1992. Oceanic Crustal Thickness from Seismic Measurements and Rare-Earth Element Inversions. J Geophys Res-Sol Ea 97, 19683-19715.
48. Wu, Z.L., Li, J.B., Ruan, A.G., Lou, H., Ding, W.W., Niu, X.W., Li, X.B., 2011. Crustal structure of the northwestern sub-basin, South China Sea: Results from a wide-angle seismic experiment. Sci China Earth Sci (in Chinese) 41, 1463-1476.
49. Zelt, C.A., Ellis, R.M., 1988. Practical and efficient ray tracing in two-dimensional media for rapid traveltime and amplitude forward modeling. Canadian Journal of Exploration Geophysics. 24, 16-31.
50. Zelt, C.A., Smith, R.B., 1992. Seismic traveltime inversion for 2-D crustal velocity structure. Geophys. J. Int. 108, 16-34.

592 51. Zhang, J., Li, J.B., Ruan, A.G., Wu, Z.L., Yu, Z.T., Niu, X.W., Ding, W.W., 2016. The
593 velocity structure of a fossil spreading centre in the Southwest Sub‐basin, South China Sea.
594 Geol J. 51, 548-561.
595 52. Zhang, M.S., 1991. Quaternary events in Xisha coral reef region. Quaternary Sciences (in
596 Chinese) 2, 165-177.
597 53. Zhao, M.H., He, E.Y., Sibuet, J.C., Sun, L.T., Qiu, X.L., Tan, P.C., Wang, J., 2018. Post-
598 Seafloor Spreading Volcanism in the Central East South China Sea and its Formation
599 Through an Extremely Thin Oceanic Crust. Geochem Geophy Geosy. 19, 621-641.
600 54. Zhu, J.J., Li, J., Sun, Z.X., Li, S.Z., 2016. Crustal thinning and extension in the northwestern
601 continental margin of the South China Sea. Geol J. 51, 286-303.
602 55. Zhu, W.L., Xie, X.N., Wang, Z.F., Zhang, D.J., Zhang, C.L., Cao, L.C., Shao, L., 2017. New
603 insights on the origin of the basement of the Xisha Uplift, South China Sea. Sci China Earth
604 Sci. 60, 2214-2222.